Spatial and temporal variability of global ocean mixing inferred from Argo profiles

C. B. Whalen,[1] L. D. Talley,[1] and J. A. MacKinnon[1]

Received 19 July 2012; accepted 27 August 2012; published 29 September 2012.

[1] The influence of turbulent ocean mixing transcends its inherently small scales to affect large scale ocean processes including water-mass transformation, stratification maintenance, and the overturning circulation. However, the distribution of ocean mixing is not well described by sparse ship-based observations since this mixing is both spatially patchy and temporally intermittent. We use strain information from Argo float profiles in the upper 2,000 m of the ocean to generate over 400,000 estimates of the energy dissipation rate, indicative of ocean mixing. These estimates rely on numerous assumptions, and do not take the place of direct measurement methods. Temporally averaged estimates reveal clear spatial patterns in the parameterized dissipation rate and diffusivity distribution across all the oceans. They corroborate previous observations linking elevated dissipation rates to regions of rough topography. We also observe heightened estimated dissipation rates in areas of high eddy kinetic energy, as well as heightened diffusivity in high latitudes where stratification is weak. The seasonal dependence of mixing is observed in the Northwest Pacific, suggesting a wind-forced response in the upper ocean. **Citation:** Whalen, C. B., L. D. Talley, and J. A. MacKinnon (2012), Spatial and temporal variability of global ocean mixing inferred from Argo profiles, *Geophys. Res. Lett.*, *39*, L18612, doi:10.1029/2012GL053196.

1. Introduction

[2] Turbulent mixing closes the ocean's energy budget by dissipating the kinetic energy originating from the winds and tides. This mixing subsequently alters water composition, changing both horizontal and vertical gradients, and thereby drives the oceanic circulation on both regional and global scales. Heat, salt, and dissolved gases are distributed throughout the ocean by mixing, both by generating signature water mass properties close to the air-sea interface and altering them in the abyssal ocean. Climate models are sensitive to the spatial and temporal structure of mixing, which has implications for their treatment of the surface ocean's heat content and subsequent atmospheric feedbacks [*Harrison and Hallberg*, 2008]. Ocean mixing can be measured by tracking a tracer [e.g., *Ledwell et al.*, 2011], or estimated from small fluctuations in temperature, conductivity, and shear measured by microstructure profilers [e.g., *Gregg et al.*, 2003]. However, these observations have limited spatial and temporal scope due to the difficult nature of the methods employed, a substantial handicap since mixing is patchy in both space and time.

[3] A growing number of observational studies indicate that internal waves are the major cause of turbulence in the ocean interior [*Alford and Gregg*, 2001; *Klymak et al.*, 2006]. Measurements reveal that the energy dissipation rate is strongly correlated with the energy of the internal wave field via a relationship consistent with wave-wave interaction theory [*Polzin et al.*, 1995; *Gregg*, 1989]. Finescale methods have been developed that either require vertical shear from velocity profiles or strain from density profiles as a measure of the internal wave energy level. Corrections are applied to account for the frequency content of the internal wave field by using the assumed constant or measured ratio between shear and strain (R_ω) along with the latitudinal dependence of the internal wave field, to form an estimate of the rate of turbulent kinetic energy dissipation ϵ [*Polzin et al.*, 1995], which can then be related to the diapycnal diffusivity κ. These finescale methods have been primarily applied to shear observations, including those from lowered acoustic Doppler current profiler (LADCP) velocity data collected on hydrographic cruises [*Kunze et al.*, 2006] with a measured R_ω correction. However, shear from ship-based hydrography measurements has limited spatial resolution (along the ship-track), and temporal resolution (every few years at best, sparse in the winter). By applying the version of this method that utilizes strain information from density profiles (the 'strain method') with a constant R_ω to a global array of Argo float profiles, we dramatically expand the reach of this technique.

[4] The few comparisons between strain-based dissipation rate estimates and those from microstructure data measured on turbulent dissipation scales [*Wijesekera et al.*, 1993] or Thorpe scale estimates derived from density overturns [*Thompson et al.*, 2007] agree within a factor of 2–3. Also, patterns in microstructure measurements of ϵ have been found to qualitatively match strain variance [*Mauritzen et al.*, 2002]. Application of this method to global hydrographic data [*Kunze et al.*, 2006] and a selection of Argo float profiles in the Southern Ocean [*Wu et al.*, 2011] has revealed patterns consistent with ship-based observations of ocean mixing. However, the strain method relies on the underlying assumptions that all observed strain is due to internal waves, and that the wave breaking rate is governed by weakly nonlinear wave-wave interactions. Therefore agreement is not always expected everywhere. For example, this method may inaccurately estimate mixing if the observed strain is caused by intrusions, or close to breaking large-amplitude internal waves [*Klymak et al.*, 2008].

[5] Here we calculate finescale strain variance from Argo float profiles, and use the strain method to estimate diapycnal mixing. Previous work has shown that these estimates are a

[1]Scripps Institution of Oceanography, University of California, San Diego, La Jolla, California, USA.

Corresponding author: C. B. Whalen, Scripps Institution of Oceanography, University of California, San Diego, 9500 Gilman Dr., Code 0208, La Jolla, CA 92037, USA. (cwhalen@ucsd.edu)

0094-8276/12/2012GL053196

good proxy for diapycnal mixing patterns [*Wijesekera et al.*, 1993; *Thompson et al.*, 2007; *Kunze et al.*, 2006; *Wu et al.*, 2011], although due to the limits of this parameterization ship-based measurements are necessary to determine accurate magnitudes at specific locations. Utilizing the strength of these estimates to show spatial and temporal patterns, we present maps of the average geographic and temporal variability, and focus on its relationship with bottom roughness, the mesoscale eddy field, and tidal energy.

2. Data and Methods

[6] The Argo program is an international effort to maintain ~3,000 freely drifting floats. Each float is equipped with conductivity, temperature, and depth (CTD) instruments that profile to 2,000 m every ten days (http://www.argo.ucsd.edu). We screened the profiles for quality, then removed the mixed layer and areas of low stratification (see auxiliary material).[1]

[7] The remaining profiles were divided into 200 m half-overlapping segments of 1–15 m resolution beginning at the bottom of each profile. The dissipation rate was estimated following *Kunze et al.* [2006], building from previous work [*Polzin et al.*, 1995; *Gregg*, 1989]. Strain ξ_z was calculated from each segment,

$$\xi_z = \frac{N^2 - N_{fit}^2}{\overline{N^2}}, \tag{1}$$

where N^2 is the buoyancy frequency derived from the potential density profile, the over-bar denotes vertical averaging, and N_{fit}^2 is a quadratic fit of the buoyancy frequency. Each strain segment was spatially Fourier transformed for the spectra S_{str}, and integrated to determine the strain variance,

$$\left\langle \xi_z^2 \right\rangle = \int_{\min(k_z)}^{\max(k_z)} S_{str}(k_z) dk_z. \tag{2}$$

The integration range was limited to wavenumbers corresponding to vertical wavelengths between 100 m and 40 m, while adjusting max (k_z) if necessary so that $\langle \xi_z^2 \rangle = <0.2$ was satisfied to avoid underestimating the variance due to spectral saturation. The corresponding value for the Garrett-Munk strain variance $\langle \xi_{zGM}^2 \rangle$ was determined over an identical wavenumber range. The Argo data do not specify whether a profile was derived from point measurements or depth averages; the latter underestimates strain variance. Following *Kunze et al.* [2006] ϵ estimates were calculated from single spectra, and were averaged together afterwards to avoid combining spectra of various vertical wavenumber resolution, but possibly overestimating the dissipation rate.

[8] This strain variance was used in the finescale parameterization for the turbulent kinetic energy dissipation rate [*Kunze et al.*, 2006],

$$\epsilon = \epsilon_0 \frac{\overline{N^2}}{N_0^2} \frac{\left\langle \xi_z^2 \right\rangle^2}{\left\langle \xi_{zGM}^2 \right\rangle^2} h(R_\omega) L(f, N), \tag{3}$$

where the constants are given by $N_0 = 5.24 \times 10^{-3}$ rad s^{-1}, $\epsilon_0 = 6.73 \times 10^{-10}$ m^2 s^{-2}. The function $L(f, N)$ provides a correction that incorporates the latitudinal dependence on the internal wave field and is defined as

$$L(f, N) = \frac{f \operatorname{arccosh}(\frac{\overline{N}}{f})}{f_{30} \operatorname{arccosh}(\frac{N_0}{f_{30}})}, \tag{4}$$

where f is the profile's Coriolis frequency, f_{30} is the Coriolis frequency at 30°, and $\overline{N}$ is the vertically averaged buoyancy frequency of the segment. The term $h(R_\omega)$ in equation (3) accounts for the frequency content of the internal wave field,

$$h(R_\omega) = \frac{1}{6\sqrt{2}} \frac{R_\omega (R_\omega + 1)}{\sqrt{R_\omega - 1}}. \tag{5}$$

Due to the lack of velocity and therefore shear data we assumed a constant value for the shear to strain ratio R_ω, choosing the Garrett-Munk value $R_\omega = 3$, a reasonable estimate for the upper 2,000 m [*Kunze et al.*, 2006]. If this choice of R_ω is an underestimate then the term $h(R_\omega)$ is also underestimated, and the converse is also true. The dissipation rate ϵ was related to the diffusivity κ by the Osborn relation [*Osborn*, 1980]

$$\kappa = \gamma \frac{\epsilon}{\overline{N^2}}, \tag{6}$$

where a mixing efficiency of $\gamma = 0.2$ was used.

[9] Smith and Sandwell ship-sounding bathymetry version 14.1 (http://topex.ucsd.edu/marine_topo/) [*Smith and Sandwell*, 1997] was used to determine bottom roughness, defined here as the variance calculated in 30 km square regions, a reasonable scale for internal tide generation [*St. Laurent and Garrett*, 2002]. The ship-sounding bathymetry was chosen over the version derived from satellite altimetry since it has higher spatial resolution. Integrated barotropic lunar semidiurnal (M_2) tidal energy was derived from the OSU Tidal Data Inversion (http://volkov.oce.orst.edu/tides/) following *Egbert and Ray* [2003]. A climatology of near-inertial mixed layer energy (http://ctoh.legos.obs-mip.fr/), along with the associated uncertainties, is explained in *Chaigneau et al.* [2008]. The eddy kinetic energy was derived from surface drifter velocity information from the Global Drifter Program (R. Lumpkin, personal communication, 2012). The time-mean version of this dataset can be found at http://www.aoml.noaa.gov/phod/dac/dac_meanvel.php [*Lumpkin and Garraffo*, 2005].

[10] Measures of uncertainty including sample size and confidence intervals, along with justification for the depth ranges used in Figures 1–4 are discussed in the auxiliary material.

3. Results

[11] Maps showing the five year mean inferred dissipation rate and diapycnal diffusivity for segments centered between 250–500 m, 500–1,000 m and 1,000–2,000 m depths are presented in Figures 1 and 2. The dissipation rate and diffusivity maps differ since they are related by the spatially varying buoyancy frequency (equation (6)). In strongly stratified regions the buoyancy frequency is large, causing lower diffusivity than at locations with a similar dissipation rate but weaker stratification. For example the Weddell Sea and Argentine Basin have similar dissipation rates, but the weaker stratification of the Weddell Sea leads to remarkably higher

[1] Auxiliary materials are available in the HTML. doi:10.1029/2012GL053196.

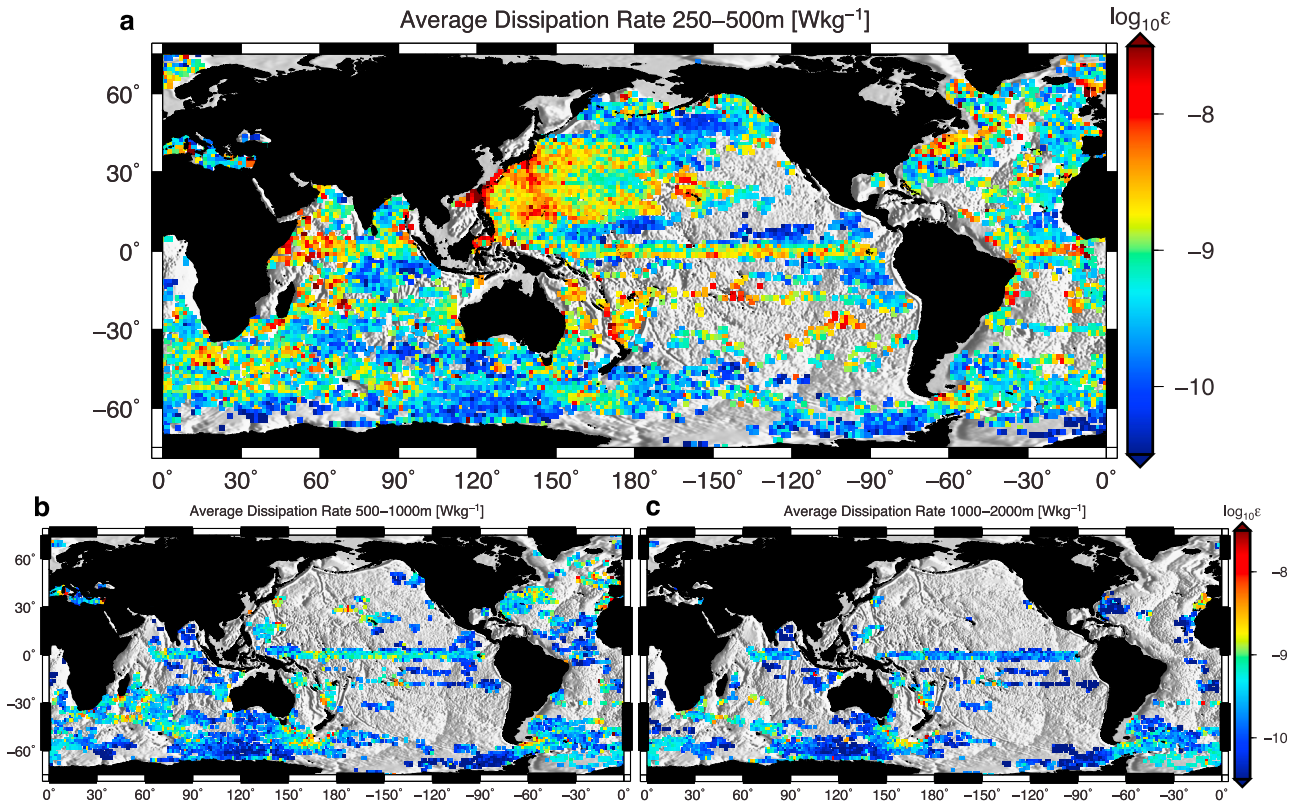

Figure 1. Dissipation rate ϵ (W kg^{-1}) estimated from over five years (2006–2011) of Argo data. Estimates from high vertical resolution data centered between (a) 250–500 m, (b) 500–1,000 m, and (c) 1,000–2,000 m are averaged over 1.5° square bins and plotted if they contain more than three dissipation rate estimates. The underlying bathymetry is from the Smith and Sandwell dataset [*Smith and Sandwell*, 1997] version 14.1.

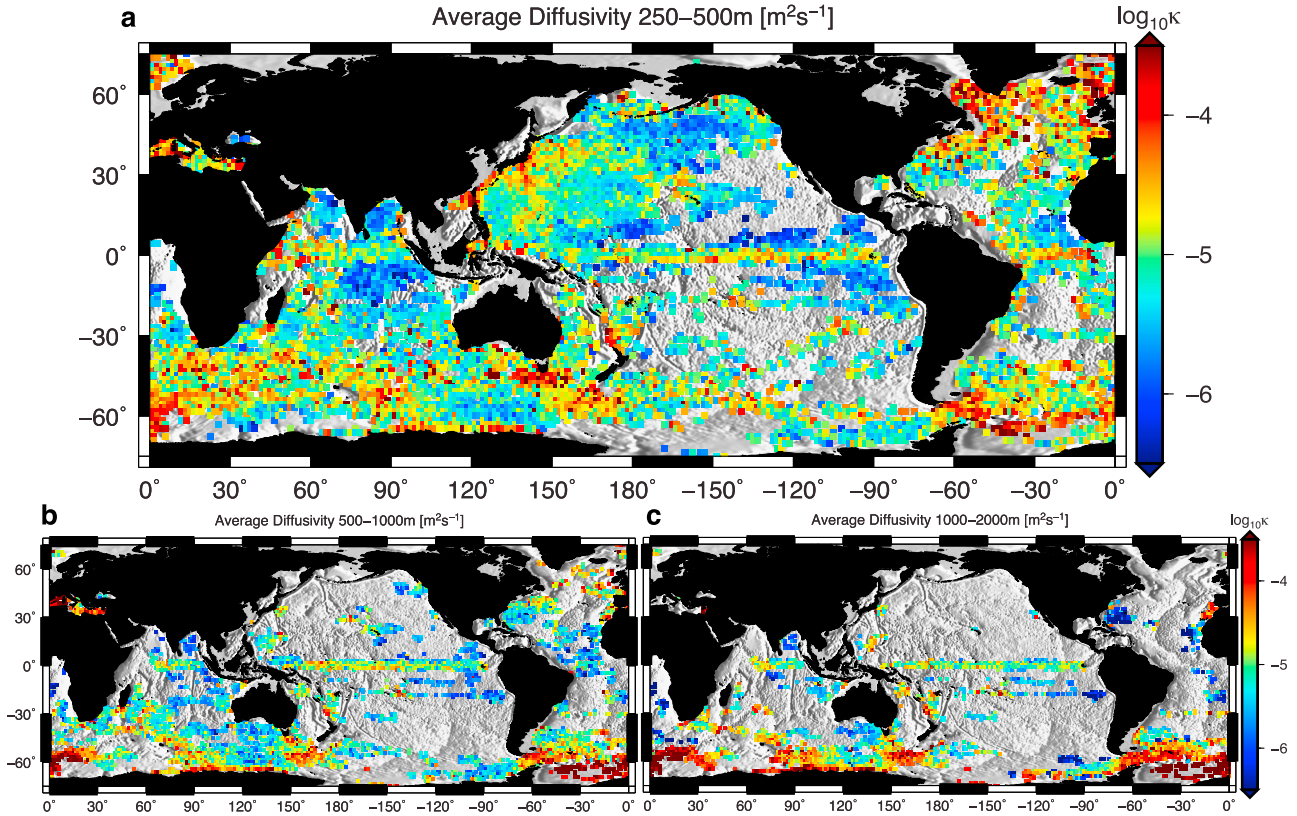

Figure 2. Averaged diffusivity κ (m^2 s^{-1}). Otherwise identical to Figure 1.

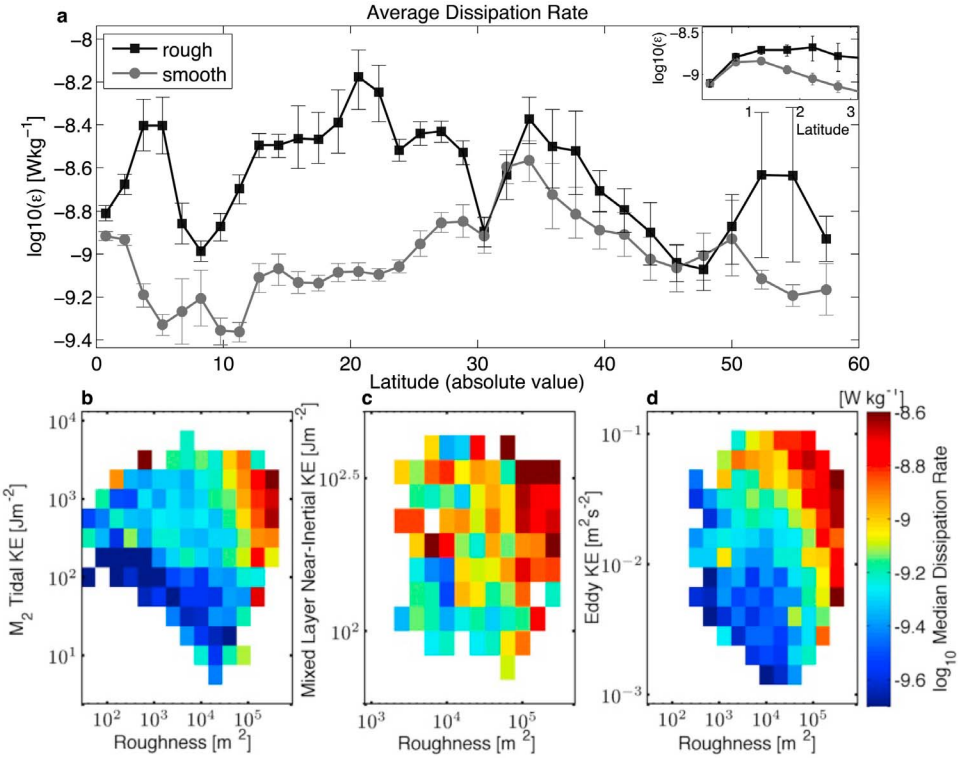

Figure 3. Dissipation related to roughness, barotropic lunar semidiurnal (M_2) tidal energy, mixed-layer near-inertial energy, and eddy kinetic energy. (a) Global mean dissipation rate for 3° half-overlapping latitudinal bands in the depth range 250–1,000 m over rough (variance greater than global mean) and smooth topography with 90% bootstrapped confidence intervals. Inset shows a finer resolution equatorial region for 1° half-overlapping bands. Median dissipation rate as a function of roughness and (b) M_2 tidal kinetic energy [*Egbert and Ray*, 2003]; (c) mixed layer near-inertial kinetic energy from *Chaigneau et al.* [2008]; and (d) eddy kinetic energy from the Global Drifter Program (R. Lumpkin, personal communication, 2012). Plotted averages include estimates between 250–1,000 m in depth for bins containing >15 estimates.

diffusivity. We find that our estimates of diffusivity and dissipation rate are related to: (1) bottom roughness, (2) tidal energy, (3) mixed layer near-inertial energy, (4) mesoscale eddy kinetic energy (EKE), and (5) proximity to the equator. Each of these are described in the following paragraphs.

[12] Both the diffusivity and dissipation rate (Figures 1 and 2) are in locally intensified over regions of rough topography (Figure S.1 in Text S1). This is true even far above the actual features, consistent with the full-depth hydrography-derived estimates of *Kunze et al.* [2006], unless the background levels are high enough to mask the mixing from rough topography. The heightened mixing may be due to local interactions between geostrophic or tidal flow and topography, such as the breaking of locally produced internal tides [*Polzin et al.*, 1997], in combination with the reflection, scattering, and breaking of remotely generated internal waves [*Johnston et al.*, 2003; *Decloedt and Luther*, 2010]. Elevated dissipation rates in Figure 1 over rough features are consistent with previous observations above the Mid-Atlantic Ridge [*Mauritzen et al.*, 2002; *Polzin et al.*, 1997], the Mendocino fracture zone in the Northeast Pacific [*Alford*, 2010], and the Southwest Indian Ridge [*Kunze et al.*, 2006]. Examples of relatively understudied areas of rough topography that have elevated mixing include the Central Indian Ridge, the Ninety East Ridge, the Chagos-Laccadive Ridge, the Sala y Gomez Fracture Zone, and the Walvis Ridge. Also notable are specific examples of reduced ϵ over smooth topographic features, including west of the Drake Passage where notably low rates of approximately 10^{-10} W kg^{-1} have been measured using tracer and microstructure methods [*Ledwell et al.*, 2011].

[13] The averaged dissipation rate is generally (but not always) higher over rougher topography than above smoother features in a latitudinal band (Figure 3a). Here we define roughness as the variance of seafloor height over 30 km scales (Figure S.1 in Text S1), and 'rough topography' as locations where this parameter exceeds the global mean. Between 5° and 30° latitude (north and south), this difference may approach an order of magnitude, while both averages also increase with latitude as previously observed [*Gregg et al.*, 2003]. Poleward of 30° the difference between ϵ over smooth and rough topography is often weaker, or not significant, indicating that at these latitudes other factors such as the magnitude of near-inertial energy input from wind may be more important in governing dissipation rate than bottom roughness.

[14] Tides are one of the energy sources for the oceanic internal wave field. The barotropic tide generates internal waves, which dissipate a portion of their energy within a few hundred kilometers of their generation site [*St. Laurent and Garrett*, 2002]. We find a correlation between elevated M_2 tidal energy, and the median dissipation rate for a given roughness level (Figure 3b). Previous observations of heightened mixing close to topographic features with strong tides are numerous, including dissipation rates exceeding 10^{-8} W kg^{-1} over the Hawaiian Ridge [*Klymak et al.*, 2006], dissipation rates reaching 2×10^{-6} W kg^{-1} in the Luzon Strait [*Alford et al.*, 2011], and diffusivity exceeding 5×10^{-4} m^2 s^{-1} in

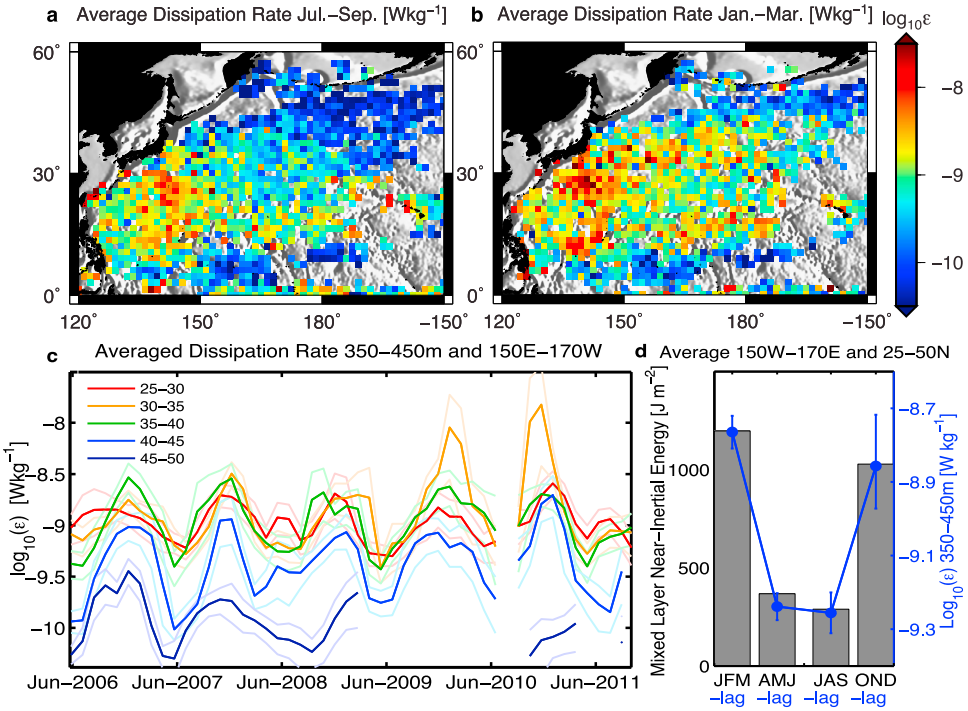

Figure 4. Seasonal cycle of the dissipation rate for the Northwest Pacific. (a, b) Spatial comparison of the winter and summer dissipation rate patterns between 350–450 m; (c) time series average of dissipation rate between 150°E and 170°W, over 5° bands of latitude, between depths of 350–450 m, with lightly colored confidence intervals; and (d) seasonally averaged mixed layer near-inertial energy in the region 150°E–170°W, 25°–50°N (gray bars) and the average dissipation rate in the same region between 350–450 m, seasonally averaged with a 50-day lag (blue line). The 90% bootstrapped confidence intervals are shown in Figures 4c and 4d.

the Brazil Basin [*Polzin et al.*, 1997]. Other notable examples of elevated dissipation rates in Figure 1 that also exhibit high tidal kinetic energy [*Egbert and Ray*, 2003] include the North Madagascar Ridge, the Southeast Bay of Bengal, the Aleutian Ridge, the Izu-Ogasawara-Mariana Ridge, South Georgia Ridge, the ridges north and south of New Zealand, and near Tahiti. Most previous in situ observations and model-derived global maps of the tidal energy dissipation rate [*St. Laurent et al.*, 2002], have highlighted mixing near rough topography in the abyssal ocean, the correlation presented here in the upper ocean is particularly striking.

[15] Wind energy contributing to the internal wave field can originate from storms and wind bursts, adding energy to the mixed layer near the inertial frequency, and triggering internal waves that dissipate energy as they propagate downward [*Alford et al.*, 2012]. Comparison of the median dissipation rate with the mixed layer near-inertial energy from *Chaigneau et al.* [2008] suggests a relationship consistent with this process. The higher the near-inertial mixed layer energy, the higher the median ϵ for a given topographic roughness (Figure 3c).

[16] The Northwest Pacific is one example of a region with both excellent Argo coverage, and notably elevated winter near-inertial mixed layer energy [*Chaigneau et al.*, 2008]. Here we find a dissipation rate that is consistently higher north of 20° during the winter (January–March) compared to the summer (July–September) (Figures 4a and 4b). The difference is especially pronounced near the Kuroshio Extension. This is consistent with the seasonal cycle of storm activity in the Pacific, resulting in internal waves and an elevated dissipation rate. Averaging our Argo-derived dissipation rate over 5° latitudinal bands between 350–450 m, 150°E and 170°W reveals a clear seasonal cycle in each band (Figure 4c). This depth range is the deepest available in this region, chosen to avoid seasonal surface stratification changes missed in the screening process. The magnitude of the average dissipation rate varies, with highest values in the band closest to the equator between 25°–30°. The seasonal cycle in mixed-layer near-inertial energy is compared with the seasonal cycle in the dissipation rate between 350–450 m and 150°E–170°W shifted 50 days later (Figure 4d). The average seasonal mixed layer near-inertial energy demonstrates a clear correlation with the delayed cycle in ϵ. Previous studies of storm-generated high mode near inertial waves [*D'Asaro et al.*, 1995] indicate that this is a reasonable time lag for these waves to propagate 400 m below the ocean surface.

[17] Areas of very high eddy kinetic energy also demonstrate a heightened dissipation rate in Figure 1 that is not directly attributable to mixing over rough topography, nor to wind or tidal energy. Comparing dissipation levels between 250–1,000 m and eddy kinetic energy values derived from surface drifter velocities (R. Lumpkin, personal communication, 2012) indicates a global relationship between the two (Figure 3d). Specific examples include, the energetic current extensions of the Gulf Stream, the Kuroshio, East Australian Current, and Agulhas. The heightened mixing in these localized areas may be due to internal waves interacting with the high concentration of eddies [*Padman et al.*, 1990; *Kunze*, 1995], internal waves generated from topography-eddy interactions [*Nikurashin and Ferrari*, 2010; *Liang and*

Thurnherr, 2012], or due to incorrectly identifying the strain associated with the eddies as internal waves. Model generated global maps of geostrophic energy input into lee waves [*Nikurashin and Ferrari*, 2011] support the eddy-topography interaction possibility for diapycnal mixing near the ocean floor, especially in the Agulhas, the eastern equatorial Pacific, and numerous locations along the Antarctic Circumpolar Current. The enhanced estimated dissipation rate in regions of high EKE between 250-1000 m suggests additional globally-relevant turbulence generation mechanisms.

[18] The equatorial band also exhibits heightened dissipation rates (Figure 1). As seen in the Figure 3a detail, the finer horizontal resolution reveals a dissipation rate maximum not at the equator, but 1–2 degrees away. This behavior is expected from the applied method's incorporation of internal waves' latitudinal dependence. However, since not all strain close to the equator is internal wave driven, these estimates maybe higher or lower than the actual equatorial dissipation rate. For example, stacked equatorial jets can create density 'steps,' within the vertical length scales that are used to estimate the dissipation rate.

4. Final Remarks

[19] The diffusivity and dissipation rate estimates shown here are unprecedented in their global coverage. We see clear spatial and temporal patterns spanning a significant portion of the ocean. The method used allows us to explore global correlations between diapycnal mixing estimates and environmental variables including the tidal, wind and eddy kinetic energy fields along with topographic roughness. This broad spatial scale treatment of diapycnal mixing can assist in the development of spatially dependent mixing parameterizations in climate models, working towards a better representation of processes such as water mass transformation, and the overturning circulation. Additionally, the estimates can be used to help guide future ship-based microstructure or tracer observations, and refine climate modeling efforts to improve our understanding of the distributions and effects of ocean mixing. As the Argo program continues to deploy floats reporting at high vertical resolution (2 m), our temporal and spatial resolution of these mixing estimates will continue to improve.

[20] **Acknowledgments.** Funding for this research was provided by NSF Ocean Sciences grant OCE-0927650. We would like to acknowledge the International Argo Program. Thanks to Alexis Chaigneau for providing the near-inertial mixed layer energy product, Rick Lumpkin for the eddy kinetic energy product, Dean Roemmich and David Sandwell for helpful discussions, and two reviewers who improved this paper by offering thoughtful comments.

[21] The Editor thanks two anonymous reviewers for assisting in the evaluation of this paper.

References

Alford, M. H. (2010), Sustained, full-water-column observations of internal waves and mixing near Mendocino Escarpment, *J. Phys. Oceanogr.*, *40*, 2643–2660.

Alford, M. H., and M. C. Gregg (2001), Near-inertial mixing: Modulation of shear, strain and microstructure at low latitude, *J. Geophys. Res.*, *106*, 16,947–16,968.

Alford, M. H., et al. (2011), Energy flux and dissipation in Luzon Strait: Two tales of two ridges, *J. Phys. Oceanogr.*, *41*, 2211–2222.

Alford, M. H., M. F. Cronin, and J. M. Klymak (2012), Annual cycle and depth penetration of wind-generated near-inertial internal waves at Ocean Station Papa in the northeast Pacific, *J. Phys. Oceanogr.*, *42*, 889–909.

Chaigneau, A., O. Pizarro, and W. Rojas (2008), Global climatology of near-inertial current characteristics from Lagrangian observations, *Geophys. Res. Lett.*, *35*, L13603, doi:10.1029/2008GL034060.

D'Asaro, E. A., C. C. Eriksen, M. D. Levine, P. Niiler, C. A. Paulson, and P. Vanmeurs (1995), Upper-ocean inertial currents forced by a strong storm. I: Data and comparisons with linear-theory, *J. Phys. Oceanogr.*, *25*, 2909–2936.

Decloedt, T., and D. S. Luther (2010), On a simple empirical parameterization of topography-catalyzed diapycnal mixing in the abyssal ocean, *J. Phys. Oceanogr.*, *40*, 487–508.

Egbert, G. D., and R. D. Ray (2003), Semi-diurnal and diurnal tidal dissipation from TOPEX/Poseidon altimetry, *Geophys. Res. Lett.*, *30*(17), 1907, doi:10.1029/2003GL017676.

Gregg, M. C. (1989), Scaling turbulent dissipation in the thermocline, *J. Geophys. Res.*, *94*, 9686–9698.

Gregg, M. C., T. B. Sanford, and D. P. Winkel (2003), Reduced mixing from the breaking of internal waves in equatorial waters, *Nature*, *422*, 513–515.

Harrison, M. J., and R. W. Hallberg (2008), Pacific subtropical cell response to reduced equatorial dissipation, *J. Phys. Oceanogr.*, *38*, 1894–1912.

Johnston, T. M. S., M. A. Merrifield, and P. E. Holloway (2003), Internal tide scattering at the Line Islands Ridge, *J. Geophys. Res.*, *108*(C11), 3365, doi:10.1029/2003JC001844.

Klymak, J. M., J. N. Moum, J. D. Nash, E. Kunze, J. B. Girton, G. S. Carter, C. M. Lee, T. B. Sanford, and M. C. Gregg (2006), An estimate of tidal energy lost to turbulence at the Hawaiian Ridge, *J. Phys. Oceanogr.*, *36*, 1148–1164.

Klymak, J. M., R. Pinkel, and L. Rainville (2008), Direct breaking of the internal tide near topography: Kaena Ridge, Hawaii, *J. Phys. Oceanogr.*, *38*, 380–399.

Kunze, E. (1995), The energy-balance in a warm-core rings near-inertial critical layer, *J. Phys. Oceanogr.*, *25*, 942–957.

Kunze, E., E. Firing, J. M. Hummon, T. K. Chereskin, and A. M. Thurnherr (2006), Global abyssal mixing inferred from lowered ADCP shear and CTD strain profiles, *J. Phys. Oceanogr.*, *36*, 1553–1576.

Ledwell, J. R., L. C. St. Laurent, J. B. Girton, and J. M. Toole (2011), Diapycnal mixing in the Antarctic Circumpolar Current, *J. Phys. Oceanogr.*, *41*, 241–246.

Liang, X., and A. Thurnherr (2012), Eddy-modulated internal waves and mixing on a midocean ridge, *J. Phys. Oceanogr.*, *42*, 1242–1248.

Lumpkin, R., and Z. Garraffo (2005), Evaluating the decomposition of tropical Atlantic drifter observations, *J. Atmos. Oceanic Technol.*, *22*, 1403–1415.

Mauritzen, C., K. L. Polzin, M. S. McCartney, R. C. Millard, and D. E. West-Mack (2002), Evidence in hydrography and density fine structure for enhanced vertical mixing over the Mid-Atlantic Ridge in the western Atlantic, *J. Geophys. Res.*, *107*(C10), 3147, doi:10.1029/2001JC001114.

Nikurashin, M., and R. Ferrari (2010), Radiation and dissipation of internal waves generated by geostrophic motions impinging on small-scale topography: Theory, *J. Phys. Oceanogr.*, *40*, 1055–1074.

Nikurashin, M., and R. Ferrari (2011), Global energy conversion rate from geostrophic flows into internal lee waves in the deep ocean, *Geophys. Res. Lett.*, *38*, L08610, doi:10.1029/2011GL046576.

Osborn, T. R. (1980), Estimates of the local-rate of vertical diffusion from dissipation measurements, *J. Phys. Oceanogr.*, *10*, 83–89.

Padman, L., M. Levine, T. Dillon, J. Morison, and R. Pinkel (1990), Hydrography and microstructure of an Arctic cyclonic eddy, *J. Geophys. Res.*, *95*, 9411–9420.

Polzin, K. L., J. M. Toole, and R. W. Schmitt (1995), Finescale parameterizations of turbulent dissipation, *J. Phys. Oceanogr.*, *25*, 306–328.

Polzin, K. L., J. M. Toole, J. R. Ledwell, and R. W. Schmitt (1997), Spatial variability of turbulent mixing in the abyssal ocean, *Science*, *276*, 93–96.

Smith, W. H. F., and D. T. Sandwell (1997), Global sea floor topography from satellite altimetry and ship depth soundings, *Science*, *277*, 1956–1962.

St. Laurent, L., and C. Garrett (2002), The role of internal tides in mixing the deep ocean, *J. Phys. Oceanogr.*, *32*, 2882–2899.

St. Laurent, L. C., H. L. Simmons, and S. R. Jayne (2002), Estimating tidally driven mixing in the deep ocean, *Geophys. Res. Lett.*, *29*(23), 2106, doi:10.1029/2002GL015633.

Thompson, A. F., S. T. Gille, J. A. MacKinnon, and J. Sprintall (2007), Spatial and temporal patterns of small-scale mixing in Drake Passage, *J. Phys. Oceanogr.*, *37*, 572–592.

Wijesekera, H., L. Padman, T. Dillon, M. Levine, C. Paulson, and R. Pinkel (1993), The application of internal-wave dissipation models to a region of strong mixing, *J. Phys. Oceanogr.*, *23*, 269–286.

Wu, L. X., Z. Jing, S. Riser, and M. Visbeck (2011), Seasonal and spatial variations of Southern Ocean diapycnal mixing from Argo profiling floats, *Nat. Geosci.*, *4*, 363–366.